UNIVERSITÉ LAVAL

Etchless Chalcogenide Microresonators Monolithically Coupled to Silicon Photonic Waveguides

Philippe Jean, Alexandre Douaud, Vincent Michaud-Belleau, Sandra Helena Messaddeq, Jérôme Genest, Sophie LaRochelle, Younès Messaddeq, and Wei Shi

OSA Optics Letters, (accepted 16 April 2020)

© 2020 Optical Society of America. One print or electronic copy may be made for personal use only. Systematic reproduction and distribution, duplication of any material in this paper for a fee or for commercial purposes, or modifications of the content of this paper are prohibited.

Copyright (c) 2020 OSA. Personal use is permitted. For any other purposes, permission must be obtained from the Optical Society of America by emailing copyright@osa.org.

Etchless Chalcogenide Microresonators Monolithically Coupled to Silicon Photonic Waveguides

Philippe Jean[1,2], **Alexandre Douaud**[1,3], **Vincent Michaud-Belleau**[1,2], **Sandra Helena Messaddeq**[1], **Jérôme Genest**[1,2], **Sophie LaRochelle**[1,2], **Younès Messaddeq**[1,4], **and Wei Shi**[1,2,*]

[1] *Centre d'Optique, Photonique et Laser (COPL), 2375 rue de la Terrasse, Université Laval, Québec, G1V 0A6, Canada*
[2] *Département de Génie Électrique et de Génie Informatique*
[3] *Département de Chimie*
[4] *Département de Physique, de Génie Physique et d'Optique, Université Laval, 2325, rue de l'Université, Québec, G1V 0A6, Canada*
[*] *Corresponding author: wei.shi@gel.ulaval.ca*

Compiled April 15, 2020

Integration of chalcogenide waveguides in silicon photonics can mitigate the prohibitive nonlinear losses of silicon while leveraging the mature CMOS-compatible nanophotonic fabrication process. In this work, we demonstrate, for the first time, a method of integrating high-Q chalcogenides microring resonators onto the silicon photonics platform without post-process etching. The method uses micro-trench filling and a novel thermal dewetting technique to form low-loss chalcogenide strip waveguides. The microrings are integrated directly inside silicon photonic circuits through evanescent coupling, providing an uncomplicated hybrid integration scheme without the need to modify the existing photonics foundry process. The microrings show a high quality factor exceeding 6×10^5 near 1550 nm and propagation losses below 0.7 dB/cm, indicating a promising solution for low-cost, compact nonlinear photonic devices with applications in various fields such as telecommunications and spectroscopy. © 2020 Optical Society of America

http://dx.doi.org/10.1364/ao.XX.XXXXXX

Research in integrated nonlinear optics has thrived in the last decade or so, thanks in part to the fast-paced improvement of nanophotonics fabrication. Various materials ranging from silicon nitride to lithium niobate are now amenable to planar integration with sub-micron features and low-loss. These advances enable new possibilities for harnessing on-chip nonlinearities such as the generation of frequency combs from parametric gain [1], Brillouin photonics [2] and Raman lasing [3]. Meanwhile, silicon-on-insulator (SOI) is regarded as the platform of choice for developing commercial applications due to its unmatched density of integration, low-cost and mature photonics components library but still falls short of other materials for nonlinear photonics and on-chip lasers. This drawback of SOI is mainly due to silicon multiphoton absorption and free-carrier generation, which result in prohibitive losses even at moderate powers [4]. To alleviate this issue, backend hybrid integration of chalcogenide glasses has been proposed as these materials combine strong nonlinearity with negligible nonlinear absorption. Furthermore, they display other interesting properties such as high rare-earth solubility for amplifiers or lasers [5], photosensitivity for reconfigurable filters [6] and transmission in the mid-infrared for biochemical sensing [7]. Co-integration of chalcogenide and silicon waveguides was previously used to enable compact Brillouin devices [8, 9]. Approaches relying on lithography and etching of the chalcogenide waveguides increase the number of post-process steps and the complexity as most photoresist developers attack the glass. Direct deposition of chalcogenide on silicon slot waveguides was also proposed for hybrid waveguides with engineered nonlinearities [10]. Alternatively, a micro-trench filling method can alleviates the requirement to etch the glass. This method was successfully used to integrate oxide glasses with silicon circuits [11, 12].

In this Letter, we propose and demonstrate an approach to integrate chalcogenide microring resonators (MRR) with silicon photonics. The MRR waveguides are formed by etching micro-trenches in the top silica cladding and filling them with chalcogenide. This method avoids directly etching the brittle chalcogenide glass and thus simplifies the post-processing steps. Moreover, a high-temperature annealing is used to induce dewetting of the glass film and create a uniform and smooth strip waveguide inside the trench. To the best of our knowledge, this is the first demonstration of optical waveguide fabrication enabled by the process of dewetting. This fabrication process results in microresonators with quality factors (Q) in excess of 6×10^5, corresponding to waveguides with propagation loss below $0.7\,\mathrm{dB \cdot cm^{-1}}$. The MRR are interfaced to silicon circuits through evanescent coupling from a tapered silicon bus waveguide. A schematic of a hybrid microresonator with radius R made of a chalcogenide waveguide of width w is shown in Fig. 1(a). The distance between the silicon bus nanowire and the ring g can be designed to control the coupling strength.

The fabrication steps are depicted in Fig. 1(b), where the silicon strip waveguide is depicted in red and the chalcogenide layer in orange. In step (1), standard photolithography pro-

National Science and Engineering Research Council of Canada (NSERC) Funding: STPGP 494358-16

Copyright (c) 2020 OSA. Personal use is permitted. For any other purposes, permission must be obtained from the Optical Society of America by emailing copyright@osa.org.

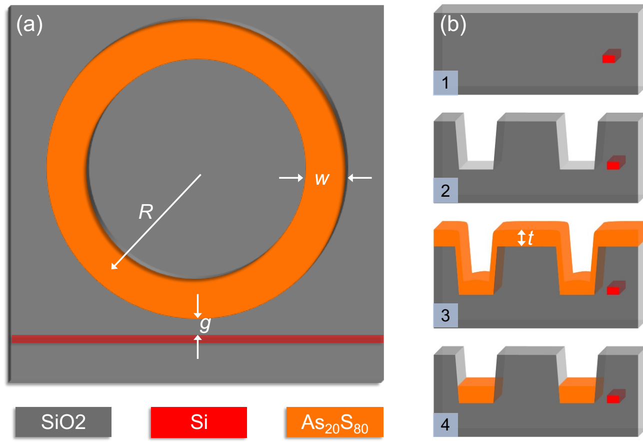

Fig. 1. (a) Top view schematic of the hybrid microresonator of radius R, waveguide width w and gap distance g. (b) Simplified process flow showing (1,2) in-foundry definition of the silicon waveguides and silica micro-trench and (3,4) in-house post-processing including the deposition of a layer of chalcogenide of thickness t and thermally induced dewetting.

cessing of the chips was done in-foundry (AMF Singapore) on 220 nm SOI wafers. In step (2), 3 µm-deep ring structures were etched in the top silica cladding to act as moulds for the glass. The following steps were performed at COPL. Between steps (2) and (3), the samples were treated to a short buffered oxide etch (10:1 BOE) dip in an effort to mitigate the sidewall roughness of the silica micro-trench. In step (3), a thin film of $As_{20}S_{80}$ with thickness t was deposited using a Nanochrome IntlVac electron beam evaporator. The evaporation chamber was evacuated down to approximately 10^{-6} Torr, and an evaporation rate of 10 Å $\cdot$ s^{-1} was used. Finally, in step (4), the samples were annealed at high temperatures under inert environment (N_2/Ar) for 120 s to induce dewetting of the film (Fig. 2(d-g)). The refractive index of the $As_{20}S_{80}$ thin film was measured using a prism coupling method. The refractive index at 1538 nm was $n = 2.1401$ after deposition and $n = 2.1658$ after annealing, indicating a slight densification of the material. Annealing temperatures ranging from 220 °C to 300 °C were studied. The annealing at 220 °C resulted in a weak dewetting and a non-uniform waveguide inside the micro-trench (Fig. 2(e)). On the other hand, higher temperature led to wider retraction of the film, up to about 100 µm at 300 °C. Energy dispersive X-ray spectroscopy (EDX) revealed a loss of sulphur as the temperature exceeded 260 °C (Fig. 2(g)). Thus, the sample annealed at 240 °C for 120 s (Fig. 2(a-c,f)) was chosen for further measurements and is referred to by default for the remainder of the text.

The $As_{20}S_{80}$ glass was prepared by the usual melt-quenching technique, from high purity arsenic (7N) and sulphur (5N), sealed in an evacuated silica tube, which was then heated at 675 °C for 12 h and air-quenched. The glass was annealed at 70 °C for about 8 h to prevent internal stresses. The $As_{20}S_{80}$ composition was chosen for its high content of sulphur. Contrary to the As_2S_3 glass whose structure is rather reticulated and comprised of $AsS_{3/2}$ pyramidal units connected by bridging sulphurs, $As_{20}S_{80}$ contains several sulphur-rich units like free S_8 rings and $AsS_{3/2}$ pyramidal units connected through S_n chains with $n \geq 2$ [13]. The presence of S_8 rings and S_n chains in the glass molecular structure induces a quasi-polymeric behaviour towards thermal treatments: a pronounced decrease in viscosity allowing higher kinetics of matter diffusion *i.e.* dewetting of the thin film [14]. As the annealing temperature surpasses the glass transition temperature, the viscosity falls dramatically, allowing a reflow of the glassy thin film driven by interfacial forces. This leads to a spontaneous reorganization of the film shape inside and around the micro-trench. This process of dewetting was previously studied as a low-cost means to fabricate microlens arrays and metasurfaces [14, 15].

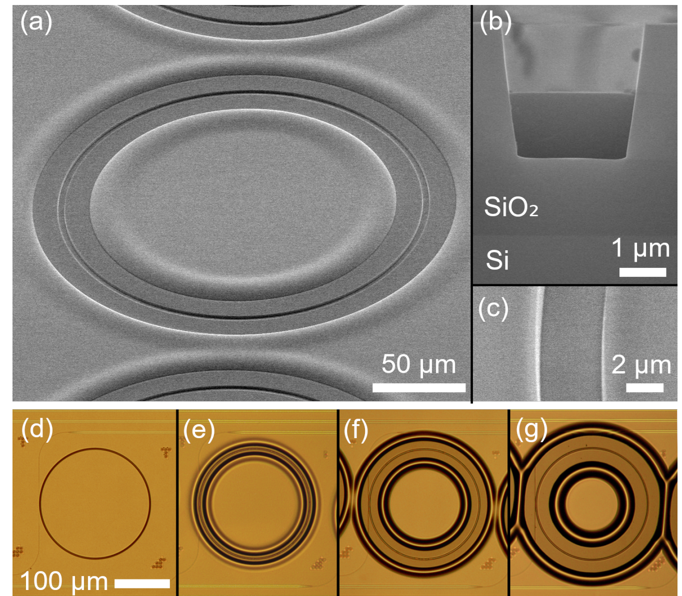

Fig. 2. SEM images of the fabricated microresonators after annealing at 240 °C for 120 s from a (a) top-view, (b) cross-section, and (c) zoomed-in top-view, and optical microscope images of the (d) as-deposited $As_{20}S_{80}$ thin film and after thermal treatments at (e) 220 °C, (f) 240 °C, and (g) 260 °C, for 120 s.

Fig. 2 shows SEM images of the fabricated MRR with a deposited thin film of thickness $t = 1.5$ µm. The presence of the etched microring led to a preferential direction for the glass flow, resulting in the formation of patterned circular structures at a distance of about 20 µm from the micro-trench, as shown in Fig. 2(a) and (f). If needed, the residual layer could be removed by a chemical-mechanical polishing (CMP) step. The reflow of the glass inside the micro-trench resulted in a highly uniform and smooth strip waveguide as can be seen in Fig. 2(b) and (c), which show the fabricated waveguide cross-section and top view, respectively. We note that the structures formed by the dewetting process result in smooth surfaces, which could play a role in developing ultra-low loss chalcogenide components in the near future.

The optical transmission of the MRR was measured in the C+L bands using an optical vector analyzer (OVA) from LUNA. The characterized samples had a width $w = 2.0$ µm and radius $R = 100$ µm. The silicon bus waveguide width was tapered down from 500 to 350 nm over 30 µm to enhance coupling with the MRR. Light was coupled to and from the chip using 100 µm-long inverted nanotapers with 180 nm tip width coupled to tapered fibers with a spot size of 2.5 µm. On-chip routing was done using 500 nm-wide single-mode rib waveguides to reduce on-chip propagation loss and mitigate backscattering. The fiber-to-waveguide insertion loss was estimated at around 5 dB.

National Science and Engineering Research Council of Canada (NSERC) Funding: STPGP 494358-16

Copyright (c) 2020 OSA. Personal use is permitted. For any other purposes, permission must be obtained from the Optical Society of America by emailing copyright@osa.org.

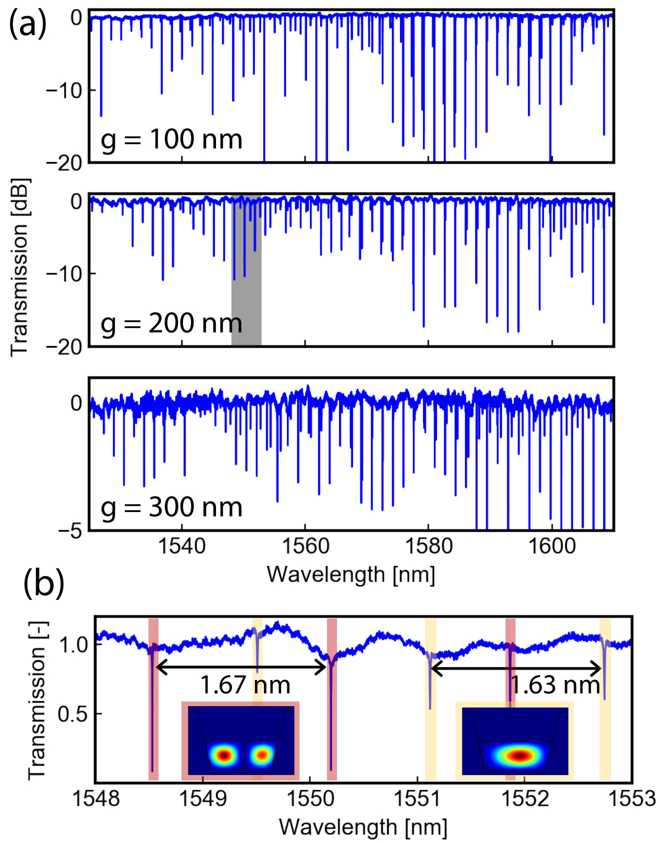

Fig. 3. (a) Normalized transmission of the microresonator with gaps of (top to bottom) 100 nm, 200 nm, and 300 nm. The shaded region is expanded in (b) to show the normalized transmission around 1550 nm with two azimuthal mode family identified. The insets of figure (b) show the simulated electric field intensity of the modes associated with the observed resonances.

The normalized MRR TE-like responses for three different coupler gaps are shown in Fig. 3(a) (top to bottom: 100 nm, 200 nm, 300 nm). The gap distances indicated on Fig. 3(a) correspond to the mask alignment values. The vertical sidewall angle combined with the deep etching (3 µm) led to a systematic gap increase of approximately 200 nm in the fabricated devices, leading to an overall decreased coupling from the target design. As such, all the resonances observed were in the undercoupled regime. As expected, increasing the gap resulted in a weaker coupling due to a decrease of the mode overlap between the bus and ring waveguides. In the undercoupled regime, this reduced coupling translates to a reduced extinction ratio in the spectra [16]. The strong resonance-to-resonance variations are attributed to intermodal coupling [17], as the micro-trench waveguide supports multiple modes at these wavelengths. Fig. 3(b) shows a close-up view of the shaded region of Fig. 3(a) to display the resonance structure around 1550 nm and highlights the multimode behaviour of the ring. Two modes are easily discernible, with free-spectral ranges (FSR) of 1.63 nm and 1.67 nm, respectively. The two FSR correspond to different optical path lengths inside the MRR. Therefore, the first and second order modes TE_0 and TE_1 are associated with the resonances spaced by FSR = 1.63 nm and FSR = 1.67 nm. This can be understood by considering that the the two modes experience distinct effective ring radii due to the displacement between their respective centroids. The effective indices of the transverse modes in the chalcogenide waveguides were simulated at 1538 nm using a finite difference eigenmode (FDE) solver, yielding values of $n_{eff} = 2.097$ and $n_{eff} = 2.020$ for the first and second TE-like modes, respectively. In contrast, the 350 nm wide silicon bus waveguide supports a single mode with index of $n_{bus} = 2.072$. The two first order modes of the ring are therefore well phase-matched with the excitation mode in the bus. We note that, according to simulations, the ring waveguide supports higher-order modes which are not excited by the bus mode because of the strong phase mismatch ($n_{eff} = 1.961$) and weak mode overlap. The simulated electric field intensity of the first two transverse TE-like modes are shown as inset in Fig. 3(b). The variations between the extinction ratios of the two modes are attributed to a combination of different modal losses and different coupling strengths.

The data presented in Fig. 3 was then used to calculate the free-spectral range (FSR). The results for the microresonator with $g = 200$ nm are summarized in Fig. 4 with the raw data points (dots and squares) and their associated linear fits (dashed line). The FSR shows an overall linear trend, increasing with the wavelength for both modes with the exception of a few points that deviates from the linear fit. Furthermore, the region near 1585 nm exhibits crossing of the two curves. These suggest the existence of strong intermodal interaction as the resonance wavelengths of the the TE_0 and TE_1 modes approach each other, resulting in potential avoided mode-crossings [17]. The regions of avoided mode-crossings could be studied more precisely using microrings with longer optical path length, leading to a decreased FSR, and more data points around the crossing frequency. The inset of Fig. 4 shows the group index n_g calculated from the FSR using FSR= $\frac{\lambda^2}{n_g 2\pi R}$ around 1585 nm. Large variations of the group index around 1585 nm indicate a modified dispersion in this region. It is noteworthy to mention that, although intermodal interactions are detrimental in certain applications, they enable the engineering of localized regions of anomalous dispersion in otherwise normal dispersion microresonators [17].

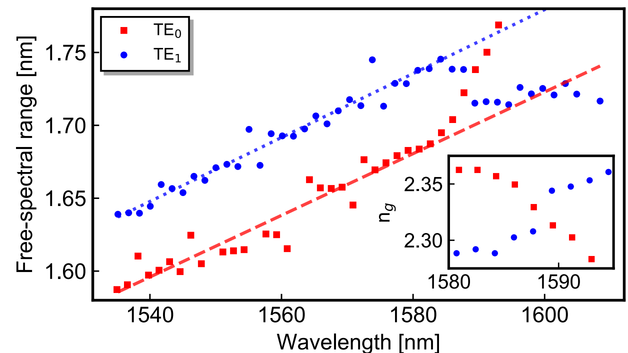

Fig. 4. Measured free-spectral range for TE_0 (red squares) and TE_1 (blue dots) modes of the microresonator. The dashed lines show linear fits of the data. The inset shows the group index calculated from the FSR data.

The OVA used to measure the data shown in Fig. 3 and 4 works on a relatively sparse wavelength grid of 1.25 pm, limited by the internal reference interferometer and proprietary processing, which proved insufficiently precise to properly fit the narrower resonances boasting pm-scale linewidths. Therefore, a simple direct absorption spectroscopy measurement was

National Science and Engineering Research Council of Canada (NSERC) Funding: STPGP 494358-16

Copyright (c) 2020 OSA. Personal use is permitted. For any other purposes, permission must be obtained from the Optical Society of America by emailing copyright@osa.org.

used to map the microresonators resonances on a finer wavelength grid. For this purpose, the output of a tunable laser (LUNA Phoenix 1400) was split and sent through the chip and to a reference quadrature fiber Mach-Zehnder interferometer to measure the chirp nonlinearities [18]. The laser was scanned at $100\,\mathrm{nm\cdot s^{-1}}$ over a 24 nm range and the output power was measured with an amplified photodetector (Thorlabs PDB430C) and a digital oscilloscope (Teledyne LeCroy WaveRunner 640Zi). Non-uniformities in the laser frequency sweep were corrected through resampling using data from the reference interferometer during post-processing. Fig. 5 shows an undercoupled resonance measured using this method for a microresonator with a gap of $g = 300\,\mathrm{nm}$. The resonance was fitted using a Lorentzian function to extract a linewidth of $\delta\lambda = 2.64\,\mathrm{pm}$. The loaded Q of the microresonator is then calculated using $Q = \lambda_0/\delta\lambda$, yielding a value slightly over 5.82×10^5. This value includes contributions from the intrinsic Q (Q_i) arising from propagation loss inside the ring waveguide as well as the extrinsic Q (Q_e) due to the coupling to the bus waveguide. The intrinsic Q can be retrieved using $Q_i = \frac{2Q}{1+\sqrt{T_0}}$ where T_0 is the transmission dip at resonance [19]. The intrinsic Q is thus estimated to be 6.02×10^5, which corresponds to waveguide propagation losses below $0.7\,\mathrm{dB\cdot cm^{-1}}$.

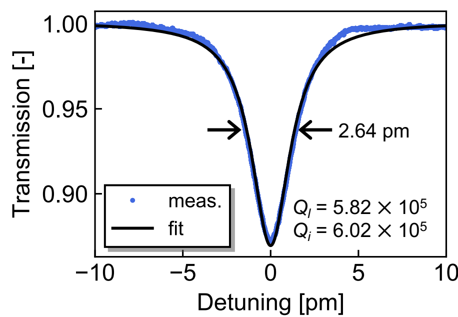

Fig. 5. Measured resonance (blue dots) of the microresonator with a Lorentzian fit (black line) indicating a linewidth of 2.64 pm at a wavelength of $\lambda = 1535.79\,\mathrm{nm}$. Q_l and Q_i are the loaded and intrinsic Q-factors, respectively.

The micro-trench waveguide propagation losses of $0.7\,\mathrm{dB\cdot cm^{-1}}$ are comparable to other demonstrations of hybrid chalcogenide-silicon integrated waveguides [8, 9]. Nevertheless, they fall short of the state-of-the-art value for planar chalcogenide waveguides of $0.05\,\mathrm{dB\cdot cm^{-1}}$ measured in an etched, multimode rib waveguide [20]. Yet, requiring no glass etching, the method proposed in this work simplifies wafer-scale hybrid integration with fewer post-processing steps requiring less equipment and time. The loss discrepancy is mainly attributed to the optical mode interaction with the silica sidewall roughness not optimized towards loss reduction by the foundry. Improvement in the MRR's Q could then be achieved by known roughness reduction methods such as thermal reflow of the oxide before the chalcogenide glass deposition [21] or wet etching of the glass [22].

In summary, we have demonstrated a hybrid chalcogenide-silicon microresonator with a Q of 6.02×10^5. We also reported on the first fabrication of chalcogenide waveguides via thermal dewetting, enabling propagation losses of $0.7\,\mathrm{dB\cdot cm^{-1}}$. Additionally, further improvement in the fabrication process should enable higher Q-factors and open the way to new nonlinear optical sources such as Raman or Brillouin lasers and Kerr soliton combs. These hybrid laser sources may benefit from the vast array of functionalities already achieved on SOI, such as power splitting-combining, polarization management, filtering and even high-speed modulation and photodetection, for more complex applications.

FUNDING INFORMATION

National Sciences and Engineering Research Council (STPGP 494358-16); Sentinel North program of Université Laval, a Canada First Research Excellence Fund.

DISCLOSURES

The authors declare no conflicts of interest.

REFERENCES

1. A. L. Gaeta, M. Lipson, and T. J. Kippenberg, Nat. Photonics **13**, 158 (2019).
2. B. J. Eggleton, C. G. Poulton, P. T. Rakich, M. J. Steel, and G. Bahl, Nat. Photonics (2019).
3. P. Latawiec, V. Venkataraman, M. J. Burek, B. J. M. Hausmann, I. Bulu, and M. Lončar, Optica **2**, 924 (2015).
4. Q. Lin, O. J. Painter, and G. P. Agrawal, Opt. Express **15**, 16604 (2007).
5. K. Yan, K. Vu, R. Wang, and S. Madden, Opt. Express **24**, 23304 (2016).
6. B. Shen, H. Lin, S. Sharif Azadeh, J. Nojic, M. Kang, F. Merget, K. A. Richardson, J. Hu, and J. Witzens, ACS Photonics **7**, 499 (2020).
7. P. Ma, D.-Y. Choi, Y. Yu, X. Gai, Z. Yang, S. Debbarma, S. Madden, and B. Luther-Davies, Opt. Express **21**, 29927 (2013).
8. B. Morrison, A. Casas-Bedoya, G. Ren, K. Vu, Y. Liu, A. Zarifi, T. G. Nguyen, D.-Y. Choi, D. Marpaung, S. Madden, A. Mitchell, and B. J. Eggleton, Optica **4** (2017).
9. Y. Liu, A. Choudhary, G. Ren, K. Vu, B. Morrison, A. Casas-Bedoya, T. G. Nguyen, D.-Y. Choi, P. Ma, A. Mitchell, S. J. Madden, D. Marpaung, and B. J. Eggleton, APL Photonics **4**, 106103 (2019).
10. S. Serna, H. Lin, C. Alonso-Ramos, C. Lafforgue, X. L. Roux, K. A. Richardson, E. Cassan, N. Dubreuil, J. Hu, and L. Vivien, Opt. Lett. **44**, 5009 (2019).
11. Z. Su, N. Li, H. C. Frankis, E. S. Magden, T. N. Adam, G. Leake, D. Coolbaugh, J. D. B. Bradley, and M. R. Watts, Opt. Express **26**, 11161 (2018).
12. J. D. B. Bradley and E. S. Hosseini, Opt. Express **22**, 12226 (2014).
13. F. Kyriazis, A. Chrissanthopoulos, V. Dracopoulos, M. Krbal, T. Wagner, M. Frumar, and S. Yannopoulos, J. Non-Cryst. Solids **355**, 2010 (2009).
14. A. Douaud, S. H. Messaddeq, and Y. Messaddeq, J. Mater. Sci. Mater. Electron. **28**, 6989 (2017).
15. D. Gentili, G. Foschi, F. Valle, M. Cavallini, and F. Biscarini, Chem. Soc. Rev. **41**, 4430 (2012).
16. W. Bogaerts, P. de Heyn, T. van Vaerenbergh, K. de Vos, S. Kumar Selvaraja, T. Claes, P. Dumon, P. Bienstman, D. van Thourhout, and R. Baets, Laser Photonics Rev. **6**, 47 (2012).
17. Y. Liu, Y. Xuan, X. Xue, P.-H. Wang, S. Chen, A. J. Metcalf, J. Wang, D. E. Leaird, M. Qi, and A. M. Weiner, Optica. **1**, 137 (2014).
18. V. Michaud-Belleau, H. Bergeron, P. S. Light, N. B. Hébert, J. D. Deschênes, A. N. Luiten, and J. Genest, Metrologia. **53**, 1154 (2016).
19. L. W. Luo, G. S. Wiederhecker, J. Cardenas, and M. Lipson, Opt. Express **19**, 1328 (2010).
20. S. J. Madden, D.-Y. Choi, D. A. Bulla, A. V. Rode, B. Luther-Davies, V. Ta'eed, M. Pelusi, and B. Eggleton, Opt. Express **15**, 14414 (2007).
21. M. H. P. Pfeiffer, J. Liu, A. S. Raja, T. Morais, B. Ghadiani, and T. J. Kippenberg, Optica **5**, 884 (2018).
22. H. Lee, T. Chen, J. Li, O. Painter, and K. J. Vahala, Nat. Commun. **3** (2012).

National Science and Engineering Research Council of Canada (NSERC) Funding: STPGP 494358-16

Copyright (c) 2020 OSA. Personal use is permitted. For any other purposes, permission must be obtained from the Optical Society of America by emailing copyright@osa.org.

FULL REFERENCES

1. A. L. Gaeta, M. Lipson, and T. J. Kippenberg, "Photonic-chip-based frequency combs," Nat. Photonics **13**, 158–169 (2019).
2. B. J. Eggleton, C. G. Poulton, P. T. Rakich, M. J. Steel, and G. Bahl, "Brillouin integrated photonics," Nat. Photonics (2019).
3. P. Latawiec, V. Venkataraman, M. J. Burek, B. J. M. Hausmann, I. Bulu, and M. Lončar, "On-chip diamond raman laser," Optica **2**, 924–928 (2015).
4. Q. Lin, O. J. Painter, and G. P. Agrawal, "Nonlinear optical phenomena in silicon waveguides: modeling and applications," Opt. Express **15**, 16604 (2007).
5. K. Yan, K. Vu, R. Wang, and S. Madden, "Greater than 50% inversion in erbium doped chalcogenide waveguides," Opt. Express **24**, 23304–23313 (2016).
6. B. Shen, H. Lin, S. Sharif Azadeh, J. Nojic, M. Kang, F. Merget, K. A. Richardson, J. Hu, and J. Witzens, "Reconfigurable frequency-selective resonance splitting in chalcogenide microring resonators," ACS Photonics **7**, 499–511 (2020).
7. P. Ma, D.-Y. Choi, Y. Yu, X. Gai, Z. Yang, S. Debbarma, S. Madden, and B. Luther-Davies, "Low-loss chalcogenide waveguides for chemical sensing in the mid-infrared," Opt. Express **21**, 29927–29937 (2013).
8. B. Morrison, A. Casas-Bedoya, G. Ren, K. Vu, Y. Liu, A. Zarifi, T. G. Nguyen, D.-Y. Choi, D. Marpaung, S. Madden, A. Mitchell, and B. J. Eggleton, "Compact Brillouin devices through hybrid integration on Silicon," Optica **4** (2017).
9. Y. Liu, A. Choudhary, G. Ren, K. Vu, B. Morrison, A. Casas-Bedoya, T. G. Nguyen, D.-Y. Choi, P. Ma, A. Mitchell, S. J. Madden, D. Marpaung, and B. J. Eggleton, "Integration of brillouin and passive circuits for enhanced radio-frequency photonic filtering," APL Photonics **4**, 106103 (2019).
10. S. Serna, H. Lin, C. Alonso-Ramos, C. Lafforgue, X. L. Roux, K. A. Richardson, E. Cassan, N. Dubreuil, J. Hu, and L. Vivien, "Engineering third-order optical nonlinearities in hybrid chalcogenide-on-silicon platform," Opt. Lett. **44**, 5009–5012 (2019).
11. Z. Su, N. Li, H. C. Frankis, E. S. Magden, T. N. Adam, G. Leake, D. Coolbaugh, J. D. B. Bradley, and M. R. Watts, "High-q-factor al2o3 micro-trench cavities integrated with silicon nitride waveguides on silicon," Opt. Express **26**, 11161–11170 (2018).
12. J. D. B. Bradley and E. S. Hosseini, "Monolithic erbium- and ytterbium-doped microring lasers on silicon chips," Opt. Express **22**, 12226–12237 (2014).
13. F. Kyriazis, A. Chrissanthopoulos, V. Dracopoulos, M. Krbal, T. Wagner, M. Frumar, and S. Yannopoulos, "Effect of silver doping on the structure and phase separation of sulfur-rich As–S glasses: Raman and SEM studies," J. Non-Cryst. Solids **355**, 2010–2014 (2009).
14. A. Douaud, S. H. Messaddeq, and Y. Messaddeq, "Microstructure formation in chalcogenide thin films assisted by thermal dewetting," J. Mater. Sci. Mater. Electron. **28**, 6989–6999 (2017).
15. D. Gentili, G. Foschi, F. Valle, M. Cavallini, and F. Biscarini, "Applications of dewetting in micro and nanotechnology," Chem. Soc. Rev. **41**, 4430 (2012).
16. W. Bogaerts, P. de Heyn, T. van Vaerenbergh, K. de Vos, S. Kumar Selvaraja, T. Claes, P. Dumon, P. Bienstman, D. van Thourhout, and R. Baets, "Silicon microring resonators," Laser Photonics Rev. **6**, 47–73 (2012).
17. Y. Liu, Y. Xuan, X. Xue, P.-H. Wang, S. Chen, A. J. Metcalf, J. Wang, D. E. Leaird, M. Qi, and A. M. Weiner, "Investigation of mode coupling in normal-dispersion silicon nitride microresonators for kerr frequency comb generation," Optica. **1**, 137–144 (2014).
18. V. Michaud-Belleau, H. Bergeron, P. S. Light, N. B. Hébert, J. D. Deschênes, A. N. Luiten, and J. Genest, "Passive coherent discriminator using phase diversity for the simultaneous measurement of frequency noise and intensity noise of a continuous-wave laser," Metrologia. **53**, 1154–1164 (2016).
19. L. W. Luo, G. S. Wiederhecker, J. Cardenas, and M. Lipson, "High quality factor etchless silicon photonic ring resonators," Opt. Express **19**, 1328–1330 (2010).
20. S. J. Madden, D.-Y. Choi, D. A. Bulla, A. V. Rode, B. Luther-Davies, V. Ta'eed, M. Pelusi, and B. Eggleton, "Long, low loss etched as2s3 chalcogenide waveguides for all-optical signal regeneration," Opt. Express **15**, 14414–14421 (2007).
21. M. H. P. Pfeiffer, J. Liu, A. S. Raja, T. Morais, B. Ghadiani, and T. J. Kippenberg, "Ultra-smooth silicon nitride waveguides based on the Damascene reflow process: fabrication and loss origins," Optica **5**, 884 (2018).
22. H. Lee, T. Chen, J. Li, O. Painter, and K. J. Vahala, "Ultra-low-loss optical delay line on a silicon chip," Nat. Commun. **3** (2012).

National Science and Engineering Research Council of Canada (NSERC) Funding: STPGP 494358-16